Spatiotemporal Metabolic Network Models Reveal Complex Autotroph-Heterotroph Biofilm Interactions Governed by Photon Incidences

Poonam Phalak[1], Hans C. Bernstein[2,3], Stephen R. Lindemann[4,5], Ryan S. Renslow[6], Dennis G. Thomas[6], Michael A. Henson[1], Hyun-Seob Song[7,8,*]

[1]*Department of Chemical Engineering and Institute for Applied Life Sciences, University of Massachusetts, Amherst, MA, United States*

[2]*Faculty of Biosciences, Fisheries and Economics, UiT - The Arctic University of Norway, Tromsø, Norway*

[3]*The Arctic Centre for Sustainable Energy (ARC), UiT - The Arctic University of Norway, Tromsø, Norway*

[4]*Whistler Center for Carbohydrate Research, Department of Food Science, Purdue University, West Lafayette, IN, United States*

[5]*Department of Nutrition Science, Purdue University, West Lafayette, IN, United States*

[6]*Biological Sciences Division, Pacific Northwest National Laboratory, Richland, WA, United States*

[7]*Department of Biological Systems Engineering, University of Nebraska-Lincoln, Lincoln, NE, United States*

[8]*Department of Food Science and Technology, Nebraska Food for Health Center, University of Nebraska-Lincoln, Lincoln, NE, United States*

(e-mail: hsong5@unl.edu)

Abstract: Autotroph-heterotroph interactions are ubiquitous in natural environment and play a key role in controlling various essential ecosystem functions, such as production and utilization of organic matter, cycling of nitrogen, sulfur, and other chemical elements. Understanding how these biofilm metabolic interactions are constrained in space and time remains challenging because fully predictive models designed for this purpose are currently limited. Toward filling this gap, here we developed community metabolic network models for two autotroph-heterotroph biofilm consortia (termed UCC-A and UCC-O), which share a suite of common heterotrophic members but have a single distinct photoautotrophic cyanobacterium (*Phormidesmis priestleyi str. ANA* and *Phormidium sp. OSCR*) that provides organic carbon and nitrogen sources to support the growth of heterotrophic partners. After determining model parameters by data fitting using the spatiotemporal distributions of microbial abundances, we comparatively analyzed the resulting biofilm models to examine any fundamental differences in microbial interactions between the two consortia under the variation of key environmental variables: CO_2 and photon levels. The UCC-A model predicted generally expected responses, i.e., the autotroph population increased in response to elevated levels of CO_2 and photon, followed by increase in the heterotroph population. In contrast, the UCC-O model showed somewhat complicated dynamics, e.g., higher photon incidence rates resulted in the increase in autotroph population but decrease in heterotroph population due to the lowered provision of glucose from the autotroph. A further analysis showed that species coexistence was governed by the photon incidences rather than the carbon availability for UCC-O, which was the opposite for UCC-A.

Keywords: cyanobacteria, environmental biofilms, metabolic modeling, hot lake communities, interspecies interactions

1. INTRODUCTION

Microbial communities are multi-species assemblies in which metabolically distinct cells interact with each other and form mutualistic, syntrophic, commensal, or antagonistic relationships (Ackermann, 2015; Bernstein et al., 2012; Hall-Stoodley et al., 2004; Stoodley et al., 2002)). These interactions are often complex and give rise to higher-order properties such as enhanced stability, robustness, and productivity (Song et al., 2015). The microbial community interactions are also governed by spatial relationships where multicellular assemblies often attach to surfaces and each other to form organized 3-dimensional structures, known as biofilms. In the chronic wound biofilms, for example, species interact with each other, form a robust community, and develop colonization resistance against pathogens. Bacteria in

biofilms grow at slower pace and slower growth may lead to decreased uptake of drug and other physiological changes leading to treatment failures (Siddiqui et al., 2010). Environmental microorganisms also assemble into biofilms and control production and utilization of organic matter, degradation of toxic compounds and the cycling of nitrogen, sulfur and other metals across highly organized spatial gradients (Cox et al., 2011; Stambler et al., 2007).

As a typical example, cyanobacteria and heterotrophic species in nature form stable microbial mats or biofilms by developing synergistic relationships. The cyanobacteria are photoautotrophic primary producers that convert inorganic matter with the help of light energy into useful organic compounds and oxygen, which are then consumed by the heterotrophic species in the vicinity (Song et al., 2016). Cyanobacteria also benefit from the presence of their partners because – at the simplest level – heterotrophs remineralize organic carbon to CO_2 and remove lower localized O_2 concentrations that otherwise may inhibit photoautotrophic growth of cyanobacteria (Beck et al., 2017; Bernstein et al., 2017). For controlling the dynamics of these communities, it is critical to understand how metabolic interactions between autotrophs and heterotrophs occur and, how they are constrained in space and time, and how those constraints affect community dynamics and biochemical function. Predictive mathematical models such as community metabolic networks can serve as a useful tool for this purpose.

Model microbial communities are useful tools for investigating and standardizing interspecies interactions (Zengler et al., 2019). Here, we consider a model cyanobacteria-heterotroph community that was originally sourced from a microbial mat in Hot Lake (Lindeman et al., 2013). The hot lake is meromictic, hypersaline lake harboring phototrophic microbial mat (Cole et al., 2014). The microbial community in the mat is metabolically diverse. The species abundances vary spatiotemporally. Many studies have been performed to understand the interactions within the community, species abundances, generation and utilization of various carbon sources and toxic compounds (Taffs et al., 2009; Widder et al., 2016). Due to the complex nature of the interspecies and intraspecies interactions, it is very difficult to understand and predict the dynamics of community formation and development. These communities play important role in biogeological cycle. The two unicyanobacterial consortia (UCC-A and UCC-O) considered here contain two distinct species of cyanobacteria (*Phormidesmis priestleyi str. ANA* and *Phormidium sp. OSCR* respectively) isolated from the Hot Lake phototrophic microbial mat (Cole et al., 2014). The heterotrophs were classified within *Alphaproteobacteria*, *Gammaproteobacteria*, and *Bacteroidetes*, and represented genera known to contain marine and halophilic aerobes.

In this study, we deploy both simple and more complex mathematical models to analyze and interpret the interactions within this model microbial community. Mathematical simulation is a useful tool to evaluate the growth and abundances of species in biofilm spatial structures. The main objective of this study is to develop a mathematical model to analyze the autotrophic and heterotrophic growth, to account for interspecies interactions through metabolite exchanges and

to predict spatial arrangements of the species in the biofilm. The multispecies biofilm model was validated by using experimental data available from previous study on photoautotroph-heterotroph biofilms (Cole et al., 2014). The validated model was then used to predict the important interactions for the community stability and development of metabolic niche in the environment. The model will be a useful tool to study autotrophic-heterotrophic interactions from other ecosystems and will aid bioengineering of photosynthetically driven microbial consortia for applications such as carbon capture and utilization (Schweitzer et al., 2021) as well as biofuel synthesis (Beck et al., 2017).

2. MATERIALS AND METHODS

2.1 System description

For model development, we chose microbial-mat-derived unicyanobacterial consortia previously studied by (Cole et al., 2014) in which the biofilms were grown in the tissue culture flasks, the metabolomics, dry weight, composition, total protein, and cell counts were measured. This study concluded that two consortia had distinct species of cyanobacteria which were primary producers along with nearly identical heterotrophs present in both the systems. The metabolomic study detected glucose in all the samples. Inorganic carbon was the sole carbon source supplied to the consortia. The biofilms were grown for 28 days under continuous photon flux of 35 μmol photons PAR/m²/s. The autotroph and heterotroph biomass obtained from the published study are shown in Figure 1B (UCCA) and Figure 1C (UCCO). The study concluded that UCCA produced higher autotroph biomass as compared to UCCO.
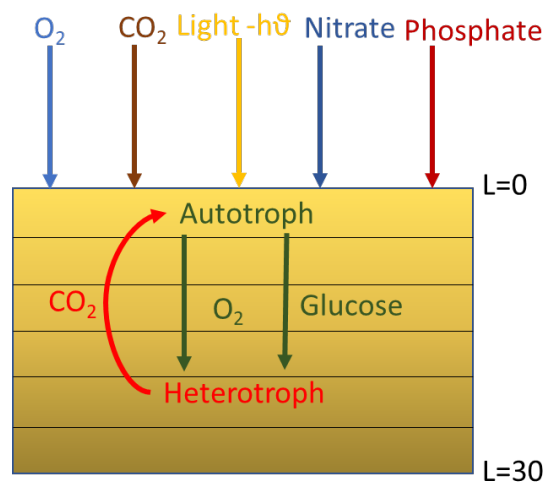

Figure 1. Schematic representation of the autotroph-heterotroph biofilm model of constant thickness L with CO_2, photon, O_2, nitrate and phosphate provided at the $L = 0$.

2.2 Model Formulation

We constructed and gapfilled core metabolic network models using U.S. Department of Energy's Systems Biology Knowledgebase (KBase) modeling platform (Arkin et al., 2018). We developed two individual networks for autotrophic cyanobacteria *Phormidesmis priestleyi ANA* and *Phormidium sp. OSCR*. The heterotroph model was generated by combining genomes of most abundant species in consortia

Bin 01 (Bacteriodetes), Bin18 (Rhodo), Bin10 (HL-49), Bin 04 (Plasmid), Bin 02 (HL-53) and Bin 05 (HL-91) (Lindemann et al., 2017). The autotroph-1 model accounts for 140 genes, 125 metabolites and 134 reactions whereas autotroph-2 model accounts for 124 genes, 137 metabolites and 139 reactions.

The core scale metabolic networks for autotrophs have been shown to provide good agreement with experimentally obtained biomass growth rates on photon and CO_2. Our preliminary flux balance calculations with maximum growth objective showed that the autotroph produced glucose and oxygen as byproducts. The heterotroph core metabolic model was examined for various glucose and oxygen uptake rates and found to be in good agreement with experimental growth rates. The major byproduct of heterotroph metabolism was CO_2.

The multispecies biofilm model was constructed for autotroph and heterotroph community in microbial mat derived unicyanobacterial consortia. The biofilm was assumed to be formed on the flask surface as described in previous publication (Cole et al., 2014), this interface was termed as bottom of the biofilm (L=30 micron) (Figure 1A). The metabolites such as inorganic carbon in the form of CO_2, O_2, nitrate and phosphate were supplied at the top of the biofilm (L=0 micron). The biofilm was assumed to be growing under constant photon incidence rate supplied at top of the biofilm. The autotrophs in the community were assumed to convert CO_2 in presence of photon energy to organic carbon (glucose) and oxygen which were consumed by heterotrophs in the community. Heterotrophs generated CO_2 as a metabolic byproduct which was consumed by autotrophs in the community. Diffusion was assumed to occur only in the axial direction of the biofilm such that spatial variations could be captured with a single variable z (Figure 1A). For simplicity, the biofilm was assumed to have a fixed thickness L over which the nutrients diffused, and cell growth occurred. Therefore, the models were most appropriate for predicting the metabolism of mature biofilms of a specified thickness.

The spatiotemporal models for photoautotroph-heterotroph consortia were constructed by combining core metabolic network models with nutrient uptake kinetics and reaction-diffusion equations for species biomass, supplied substrates and synthesizes metabolic byproducts.

The species biomass was calculated by using,

$$\frac{\partial X_i(z,t)}{\partial t} = \mu_i X_i + D_{Xi} \frac{\partial^2 X_i}{\partial z^2}$$
$$-D_{Xi} \frac{\partial X_i(0,t)}{\partial z} = k_{Xi,0} \left(X_{i,b} - X_i(0,t) \right),$$
$$-D_{Xi} \frac{\partial X_i(L,t)}{\partial z} = k_{Xi,L} \left(0 - X_i(L,t) \right) \quad (1)$$

where X_i was the biomass concentration (g/L) of i-th species. μ_i is the growth rate (h^{-1}) of the i-th species. The biomass was assumed to be diffused with diffusion coefficient (D_{Xi}) and removed from the both ends of the biofilm at the mass transfer rates ($k_{Xi,0}$ and $k_{Xi,L}$).

The metabolite concentrations (CO_2, phosphate, nitrate, glucose and oxygen) were calculated by using,

$$\frac{\partial M_j(z,t)}{\partial t} = v_{MjXi} X_i + D_{Mj} \frac{\partial^2 M_j}{\partial z^2}$$
$$-D_{Mj} \frac{\partial M_j(0,t)}{\partial z} = k_{Mj}(M_{j,b} - M_j(0,t))$$
$$-D_{Mj} \frac{\partial M_j(L,t)}{\partial z} = k_{Mj} \left(0 - M_j(L,t) \right) \quad (2)$$

where M_j was the concentration (mmol/L) of j-th metabolite (CO_2, phosphate, nitrate, glucose, O_2). The uptake fluxes v_{MjXi} of j-th metabolite for i-th species was calculated from flux balance calculations. The metabolites were assumed to be diffused at the rate of D_{Mj} and removed from the bottom of the biofilm at the mass transfer rate, k_{Mj}. M_{jb} was bulk concentration of the metabolite at the air-biofilm interface. We supplied CO_2, phosphate, nitrate and O_2 at the top of the biofilm and the accumulated metabolites were removed from both ends of the biofilm.

Uptake kinetics were specified for the four primary metabolites: CO_2, photon, glucose and oxygen. The uptake kinetics for each metabolite were assumed to follow Michaelis-Menten expressions.

$$v_i = \frac{v_{max,i} S_i}{K_{m,i} + S_i} \quad (3)$$

the uptake rate (mmol/gDW/h) of the i-th substrate, S_i is the extracellular concentration (mmol/L) of the i-th substrate, $v_{max,i}$ is the maximum uptake rate and $K_{m,i}$ is the half saturation constant. Equation (1) was used to establish transport bounds on the uptake rates with the actual uptake rates being determined by solution of the intracellular flux balance problem.

The uptake kinetics of phosphate and nitrate had the form,

$$v_p = \alpha_p \frac{v_{max,p} P}{K_{m,p} + P} \quad (4)$$

$$v_n = \alpha_n \frac{v_{max,n} N}{K_{m,n} + N} \quad (5)$$

where v_p and v_n are the uptake rates (mmol/gDW/h), P and N are the extracellular concentrations (mmol/L), $v_{max,p}$ and $v_{max,n}$ are the maximum uptake rates and $K_{m,p}$ and $K_{m,n}$ are the half saturation constants of the phosphate and nitrate respectively. Equations (2 and 3) were used to establish transport bounds on the uptake rates with the actual uptake rates being determined by solution of the intracellular flux balance problem. The parameters α_p and α_n were added to evaluate the effect of restricted phosphate and nitrate uptakes on biomass concentration and species interactions.

Attenuation of scalar incidence irradiance was calculated by using Beer-Lambert law,

$$I = I_{in} e^{-(k_{tot}(L-z))} \quad (6)$$

where I_{in} is the initial photon incident rate (µE/m^{2}s). The attenuation coefficient, k_{tot} was adjusted to achieve enough penetration of light into the biofilm. The photon incidence rate obtained from this equation was used to calculate the lower bound on photon uptake rate by using nutrient uptake kinetics. The lower bound of photon uptake rate along with other nutrient bounds were used for solving core metabolic model

and the corresponding growth rates of autotrophs were obtained.

2.3 Solving model equations

The biofilm model was consisting of a set of partial differential equations (PDEs) with mixed boundary conditions and embedded LPs. We converted those PDEs to ordinary differential equations (ODEs) by discretizing in space. The algebraic equation (AE) for photon balance equation combined with the ODEs led to system of differential algebraic equations (DAEs). The DAE system was solved using DFBAlab, a MATLAB tool that explicitly addresses problems associated with LP alternative optima and possible infeasibilities. DFBAlab employs a lexicographic optimization strategy in which a series of LP problems are sequentially solved to ensure the determination of unique exchange fluxes necessary for a well-defined dynamic system. We specified the lexicographic optimization objectives to reflect the anticipated physiology of the autotroph-heterotroph biofilm. We used 30 spatial node points to achieve fast and accurate solutions. We solved 210 ODEs, one algebraic equation for photon balance and 390 LPs in MATLAB 2017b using DFBAlab, stiff ode integrator ode15s and Gurobi 7.5.2 as a LP solver (Chen et al., 2016; Phalak et al., 2016).

2.4 Model Parameters

For determining parameter values, we used the species abundance data available at various depths in the biofilms of UCC-A and UCC-O at different times (see Figure 1B and 1C). The spatial data available for the fraction of biomass was converted to the biomass concentration at various locations by using biofilm density. The concentration of autotrophs and heterotrophs vary in space and time. We used day 7 spatial data as an initial condition for the model and validated the model for day 14, day 21 and day 28. We used least square curve (lscurvefit) fitting technique in MATLAB to fit the experimental data and validate the biofilm model. The lower bound and upper bounds on the parameters were chosen based on the available literature values. The global optimum was sought by using multistart option in MATLAB. This approach chose various starting points in from the lower and upper bounds.

The parameters used in the biofilm model are not reported here due to space limitations. The kinetic parameters (v_{max} and K_m) for the metabolites were obtained from model fitting. We have used the values obtained from literature as the initial guesses for v_{max} and K_m (Meadow s et al., 2010; Shastri et al., 2005; Triana et al., 2014). The aqueous diffusion coefficients for substrates and byproducts were converted to the biofilm diffusion coefficients using appropriate coefficients (Stewart, 2003). The diffusion coefficients and the mass transfer rate constant for biomass were obtained from the validation of the biofilm experimental data.

3. RESULTS

3.1 Biofilm model validation

The UCC-O and UCC-A biofilm models were validated by using data from an experimental study (Cole et al., 2014). The uptake kinetics for CO_2, glucose, oxygen and photon were specified with an abundant amount of nitrate and phosphate. We have used two approaches to fit the experimental data. The first approach assumed that the biofilm was grown under limited amount of CO_2, photon and oxygen and unlimited amount of nitrate and phosphate. We termed this model as unconstrained model. The other approach assumed that the biofilm was grown under limited amount CO_2, photon and oxygen but the autotroph's phosphate and/or nitrate uptakes were restricted. We termed this model as constrained model. The phosphate constraint (α_p) in the model considered limited access to the phosphate to autotrophs after day 14 as predicted by the study on autotrophs and heterotrophs (Lindemann et al., 2017). The nitrate uptake constraint ($\alpha_n = 0.75$) for autotrophs in UCC-O was added to account for their capabilities to secrete the extracellular polymeric substances. We compared the predictions from constrained and unconstrained model with the experimental data.

The unconstrained UCC-O model predicted higher autotroph and heterotroph biomass concentrations than the constrained model (Figure 2). The model fitting improved for the constrained model. The root mean least square error for constrained model reduced by 10% as compared with that for unconstrained model. The model fittings improved in presence of nitrate and phosphate limitations as this incorporates important metabolite exchanges in the system.

The UCC-O model captured the qualitative peak locations for autotrophs and heterotrophs for day 21 (Figure 2A and 2B middle panels) and day 28 (Figure 2A and 2B bottom panels). The UCC-O model predicted lower heterotroph biomass concentrations for day 14, day 21 and day 28 as compared to the experimental observation. The UCC-O model successfully captured the temporal shifts of peak locations for autotrophs and heterotrophs.
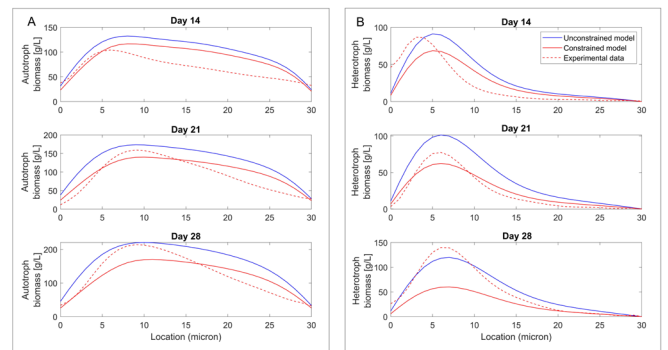

Figure 2. Spatially resolved model fitting for UCC-O autotroph-heterotroph biofilms with (constrained model, red solid lines) and without (unconstrained model, blue lines) nitrate and phosphate limitation. (A) Autotroph biomass (g/L) at day 14 (top panel), day 21(middle panel) and day 28 (bottom panel) for biofilm of thickness $L = 30$ μm. (B) Heterotroph biomass (g/L) at day 14 (top panel), day 21(middle panel) and day 28 (bottom panel) for biofilm of thickness $L = 30$ μm.

The constrained model for UCC-A assumed restricted phosphate uptakes for autotrophs after day 14. This deemed reasonable as with increase in the time, the access to available phosphate was limited. We accounted this effect by multiplying the phosphate uptake rate of autotrophs after 14 days by $\alpha_p = 1$. The optimized value of α_p was obtained from

data fitting analysis. We compared the model predictions for constrained and unconstrained case with the experimental data. The autotroph and heterotroph biomass concentrations for unconstrained model were slightly higher than that from the constrained model. We did not find any significant change in root mean square error when we compared the model predictions from constrained and unconstrained case.

Our biofilm model qualitatively captured the experimental behavior of the photoautotroph-heterotroph biofilms from hot lake (Figure 3). The UCC-A model depicted the qualitative peak locations for the day 14 (Figure 3A and 3B, top panels) and day 28 (Figure 3A and 3B, bottom panels) for autotrophs and heterotrophs. The model also captured the shifting of temporal peak locations for autotrophs and heterotrophs. The model could not successfully fit the heterotroph data for day 21 (Figure 3B, middle panel). The possible reasons for this data would be an error in experimental measurements or the lack of details in the modeling framework.
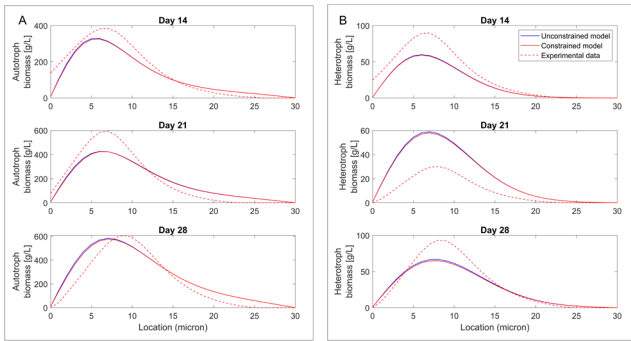

Figure 3. Spatially resolved model fitting for UCC-A autotroph-heterotroph biofilms with (constrained model, red solid lines) and without (unconstrained model, blue lines) phosphate limitation. (A) Autotroph biomass (g/L) at day 14 (top panel), day 21(middle panel) and day 28 (bottom panel) for biofilm of thickness $L = 30$ μm. (B) Heterotroph biomass (g/L) at day 14 (top panel), day 21(middle panel) and day 28 (bottom panel) for biofilm of thickness $L = 30$ μm

3.2 Effect of CO_2

The validated constrained models were used to predict the interactions between autotrophs and heterotrophs at various CO_2 concentrations under restricted phosphate and nitrate uptakes by autotrophs. Reduced nitrate and phosphate uptakes are observed during succession for UCC-O and reduced phosphate uptakes were observed for UCC-A (Lindemann et al. 2017). This effect was incorporated by adding parameters for phosphate (α_p) and nitrate (α_n) in calculation of uptakes for autotrophs. We chose various values of α_p between 0 and 1 and the respective community biomass were calculated. For UCC-A, the biomass concentration was constant for α_p=1, 0.75, 0.5 but it decreased at α_p=0.25. In case of UCC-O the biomass concentration was very sensitive to α_p, the concentration dropped with decrease in α_p. Cyanobacterium *Phormidium sp.* OSCR is known to produce more extracellular polymeric substances (EPS) than cyanobacterium *Phormidesmis priestleyi* ANA. We have accounted for this behavior by restricting nitrate uptake for autotrophs in UCC-O by setting α_n =0.75. We have considered α_p=0.25 for UCC-A and UCC-O and evaluated the effect of CO_2 concentration on community abundances. We varied the concentration of CO_2 supplied at the top of the biofilm (L=0) from 0.1 mmol/L to 10 mmol/L under the photon incidence rate of 35 μmol photons PAR/m²s. We have plotted the average biomass concentrations and average metabolite (glucose and O_2) concentrations at the end of day 14, day 21 and day 28 for UCC-A and UCC-O biofilms.

The average autotroph biomass concentrations for UCC-A increased from day 14 to day 28 for various CO_2 concentrations whereas that of heterotrophs decreased for 0.1 mM of CO_2 and increased for all other CO_2 concentrations (Figure 4E and 4F). The highest autotroph biomass concentration (222.8 g/L at 28 days) and heterotroph biomass concentration (21.7 g/L at 28 days) were obtained for CO_2 concentration 10 mM. This suggests that the CO_2 concentration played an important role in autotroph growth and biomass accumulation. Autotrophs secreted less amount of glucose for CO_2 level 0.1 mM as compared to CO_2 levels 0.5 mM and 10 mM. The accumulation of glucose at 0.1 mM of CO_2 was the least due to its faster consumption by heterotrophs. O_2 secretion increased with increase in supplied CO_2. Heterotroph growth was mainly limited by glucose secretion than that of O_2.
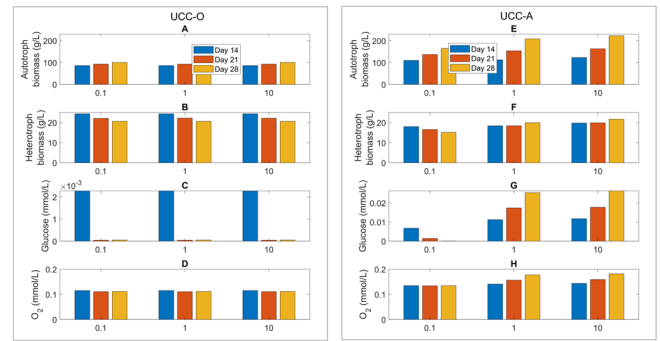

Figure 4. Predictions after 14, 21 and 28 days for UCC-O and UCC-A biofilms of thickness L = 30 μm at various CO_2 concentration and constant photon incidence (35 μmol photons PAR/m²/s). 0.1: CO_2 concentration 0.1 mmol/L. 0.5: CO_2 concentration 0.5 mmol/L. 10: CO_2 concentration 10 mmol/L. (A) UCC-O: Autotroph biomass concentrations averaged across the biofilm. (B) UCC-O: Heterotroph biomass concentrations averaged across the biofilm. (C) UCC-O: Glucose concentrations averaged across the biofilm. (D) UCC-O: Oxygen concentrations averaged across the biofilm. (E) UCC-A: Autotroph biomass concentrations averaged across the biofilm. (F) UCC-A: Heterotroph biomass concentrations averaged across the biofilm. (G) UCC-A: Glucose concentrations averaged across the biofilm. (H) UCC-A: Oxygen concentrations averaged across the biofilm.

For UCC-O, autotroph biomass concentration increased from 79.5 g/L (at day 14) to 93 g/L (at day 28) for all CO_2 concentrations considered here (Figure 4A). This indicated that the CO_2 was not a limiting substrate for autotroph growth. Exact opposite trend was observed for heterotroph biomass concentration, it decreased from 20.7 g/L (at day 14) to 17.4 g/L (at day 28) (Figure 4B). The accumulation of glucose increased from day 14 to day 28 whereas that of O_2 was constant for all CO_2 levels. The model predicted that CO_2 concentration does not significantly affect the temporal patterns of the compositional change in UCC-O.

3.3 Effect of light incidence rate

The model was further used to predict the impact of photon incidence on the community stability and dynamics. We evaluated three different photon incidence rates (10, 35 and 50 µmol photons PAR/m^2/s) at constant CO_2 concentration (10 mmol/L). The averaged species and metabolite concentrations were plotted at the end of 14, 21 and 28 days for UCC-A and UCC-O biofilms.

The autotroph concentration in case of UCC-A biofilms increased from day 14 to day 28 with increase in photon incidence rate from 10 to 50 µmol photons PAR/m^2/s (Figure 5E) with the highest concentration of 282.5 g/L was obtained at day 28 for photon incidence rate of 50 µmol photons PAR/m^2/s. The amount of glucose secreted by autotrophs increased for photon incidence rate of 10 and 35 µmol photons PAR/m^2/s but it decreased for photon incidence rate µmol photons PAR/m^2/s (Figure 5G). The amount of O_2 secreted by autotrophs increased for all photon incidence rates (Figure 5H). Heterotrophs utilized the glucose and oxygen efficiently and increased their abundances from 14 g/L (at day 28) to 21.7 g/L (at day 28) for the case of 10 and 35 µmol photons PAR/m^2/s respectively but later the abundance decreased to 20.3 g/L (at day 28) for incidence rate 50 µmol photons PAR/m^2/s (Figure 5F). This suggested that the heterotroph concentration directly depended on autotroph concentration until photon incidence rate of 35 µmol photons PAR/m^2/s but later it decreased for 50 µmol photons PAR/m^2/s. The autotroph concentration increased with increase in photon incidence rate.
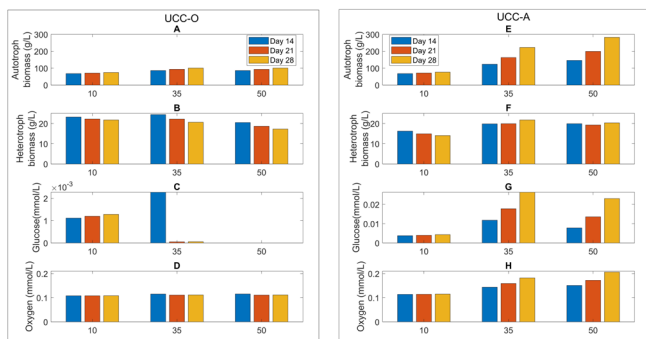

Figure 5. Predictions after 14, 21 and 28 days for UCC-O and UCC-A biofilms of thickness L = 30 µm at various photon incidence rates and constant CO_2 concentration (10 mmol/L). 10: photon incidence rate 10 µmol photons PAR/m^2/s. 35: photon incidence rate 35 µmol photons PAR/m^2/s. 50: photon incidence rate 50 µmol photons PAR/m^2/s. (A) UCC-O: Autotroph biomass concentrations averaged across the biofilm. (B) UCC-O: Heterotroph biomass concentrations averaged across the biofilm. (C) UCC-O: Glucose concentrations averaged across the biofilm. (D) UCC-O: Oxygen concentrations averaged across the biofilm. (E) UCC-A: Autotroph biomass concentrations averaged across the biofilm. (F) UCC-A: Heterotroph biomass concentrations averaged across the biofilm. (G) UCC-A: Glucose concentrations averaged across the biofilm. (H) UCC-A: Oxygen concentrations averaged across the biofilm.

The autotroph concentration in case of UCC-O biofilms increased from day 14 to day 28 with increase in photon incidence rate from 10 to 50 µmol photons PAR/m^2/s (Figure 5A) with the highest concentration of 93.1 g/L was obtained at day 28 for photon incidence rate of 35 and 50 µmol photons PAR/m^2/s. The amount of glucose accumulated decreased for photon incidence rates of 35 and 50 µmol photons PAR/m^2/s but it increased for photon incidence rate 10 µmol photons PAR/m^2/s (Figure 5C). The amount of O_2 accumulated in biofilm was constant for all photon incidence rates (Figure 5D). Heterotrophs utilized the glucose and O_2 increased their abundances initially for day 14 but it decreased due to low glucose availability. Time averaged heterotroph concentration dropped from 22.4 g/L to 18.7 g/L with increase in photon incidence rate. This suggested that the photon incidence rate positively affected the autotroph concentrations but negatively impacted the heterotroph abundances.

CONCLUSION

To study the interactions within the autotroph-heterotroph community found in unicyanobacterial consortia in microbial mat, we developed a biofilm model by coupling core metabolic networks of these two functional groups with one-dimensional reaction-diffusion equations. Our models captured the species interactions at various depths in hot lake and predicted the species abundances. The models were used to predict the effect of CO_2 and photon on interactions within the community and the species coexistence. UCC-A model predicted that the autotroph biomass increased by 35%, and the heterotroph biomass by 43% when CO_2 concentration increased from 0.1 mM to 10 mM at constant photon rate (35). This suggested that the CO_2 concentration significantly impacted the community biomass and the species interactions. In case of UCC-O community, CO_2 concentration did not change the individual biomass concentrations, suggesting that the community is robust to the change in the concentration of available carbon at constant photon rate.

REFERENCES

Ackermann, M. (2015). A functional perspective on phenotypic heterogeneity in microorganisms. *Nature Reviews Microbiology, 13*(8), 497-508.

Arkin, A. P., Cottingham, R. W., Henry, C. S., Harris, N. L., Stevens, R. L., Maslov, S., ... & Yu, D. (2018). KBase: the United States department of energy systems biology knowledgebase. *Nature Biotechnology*, 36(7), 566-569.

Beck, A. E., Bernstein, H. C., & Carlson, R. P. (2017). Stoichiometric network analysis of cyanobacterial

acclimation to photosynthesis-associated stresses identifies heterotrophic niches. *Processes*, 5(2), 32.

Beck, A. E., Hunt, K. A., Bernstein, H. C., & Carlson, R. P. (2016). Interpreting and designing microbial communities for bioprocess applications, from components to interactions to emergent properties. *In Biotechnology for biofuel production and optimization* (pp. 407-432). Elsevier.

Bernstein, H. C., & Carlson, R. P. (2012). Microbial Consortia Engineering for Cellular Factories: in vitro to in silico systems. *Computational and structural biotechnology journal, 3*(4), 1-8.

Bernstein, H. C., McClure, R. S., Thiel, V., Sadler, N. C., Kim, Y. M., Chrisler, W. B., ... & Beliaev, A. S. (2017). Indirect interspecies regulation: transcriptional and physiological responses of a cyanobacterium to heterotrophic partnership. *MSystems*, 2(2), e00181-16.

Chen, J., Gomez, J. A., Höffner, K., Phalak, P., Barton, P. I., & Henson, M. A. (2016). Spatiotemporal modeling of microbial metabolism. *BMC systems biology, 10*(1), 1.

Cole, J. K., Hutchison, J. R., Renslow, R. S., Kim, Y.-M., Chrisler, W. B., Engelmann, H. E., . . . Fredrickson, J. K. (2014). Phototrophic biofilm assembly in microbial-mat-derived unicyanobacterial consortia: model systems for the study of autotroph-heterotroph interactions. *Frontiers in microbiology, 5*, 109.

Cox, A., Shock, E. L., & Havig, J. R. (2011). The transition to microbial photosynthesis in hot spring ecosystems. *Chemical Geology, 280*(3-4), 344-351.

Hall-Stoodley, L., Costerton, J. W., & Stoodley, P. (2004). Bacterial biofilms: from the natural environment to infectious diseases. *Nature Reviews Microbiology, 2*(2), 95-108.

Lindemann, S. R., Mobberley, J. M., Cole, J. K., Markillie, L. M., Taylor, R. C., Huang, E., . . . Nelson, W. C. (2017). Predicting Species-Resolved Macronutrient Acquisition during Succession in a Model Phototrophic Biofilm Using an Integrated 'Omics Approach. *Frontiers in microbiology, 8*, 1020.

Lindemann, S. R., Moran, J. J., Stegen, J. C., Renslow, R. S., Hutchison, J. R., Cole, J. K., . . . Malfatti, S. A. (2013). The epsomitic phototrophic microbial mat of Hot Lake, Washington: community structural responses to seasonal cycling. *Frontiers in microbiology, 4*, 323.

Meadows, A. L., Karnik, R., Lam, H., Forestell, S., & Snedecor, B. (2010). Application of dynamic flux balance analysis to an industrial Escherichia coli fermentation. *Metabolic engineering, 12*(2), 150-160.

Phalak, P., Chen, J., Carlson, R. P., & Henson, M. A. (2016). Metabolic modeling of a chronic wound biofilm

consortium predicts spatial partitioning of bacterial species. *BMC systems biology, 10*(1), 90.

Schweitzer, H., Aalto, N. J., Busch, W., Chan, D. T. C., Chiesa, M., Elvevoll, E. O., ... & Bernstein, H. C. (2021). Innovating carbon-capture biotechnologies through ecosystem-inspired solutions. *One Earth*, 4(1), 49-59.

Siddiqui, A. R., & Bernstein, J. M. (2010). Chronic wound infection: facts and controversies. *Clinics in dermatology*, 28(5), 519-526.

Shastri, A. A., & Morgan, J. A. (2005). Flux balance analysis of photoautotrophic metabolism. *Biotechnology progress, 21*(6), 1617-1626.

Song, K., Tan, X., Liang, Y., & Lu, X. (2016). The potential of Synechococcus elongatus UTEX 2973 for sugar feedstock production. *Applied microbiology and biotechnology, 100*(18), 7865-7875.

Song, H. S., Renslow, R. S., Fredrickson, J. K., & Lindemann, S. R. (2015). Integrating ecological and engineering concepts of resilience in microbial communities. *Frontiers in microbiology*, 6, 1298.

Stambler, N., & Dubinsky, Z. (2007). Marine phototrophs in the twilight zone. In *Algae and cyanobacteria in extreme environments* (pp. 79-97): Springer.

Stewart, P. S. (2003). Diffusion in biofilms. *Journal of bacteriology, 185*(5), 1485-1491.

Stoodley, P., Sauer, K., Davies, D., & Costerton, J. W. (2002). Biofilms as complex differentiated communities. *Annual Reviews in Microbiology, 56*(1), 187-209.

Taffs, R., Aston, J. E., Brileya, K., Jay, Z., Klatt, C. G., McGlynn, S., . . . Inskeep, W. P. (2009). In silico approaches to study mass and energy flows in microbial consortia: a syntrophic case study. *BMC systems biology, 3*(1), 114.

Triana, J., Montagud, A., Siurana, M., Fuente, D., Urchueguia, A., Gamermann, D., . . . Urchueguia, J. F. (2014). Generation and Evaluation of a Genome-Scale Metabolic Network Model of Synechococcus elongatus PCC7942. *Metabolites, 4*(3), 680-698. doi:10.3390/metabo4030680

Widder, S., Allen, R. J., Pfeiffer, T., Curtis, T. P., Wiuf, C., Sloan, W. T., . . . Shou, W. (2016). Challenges in microbial ecology: building predictive understanding of community function and dynamics. *The ISME journal, 10*(11), 2557.

Zengler, K., Hofmockel, K., Baliga, N. S., Behie, S. W., Bernstein, H. C., Brown, J. B., ... & Northen, T. R. (2019). EcoFABs: advancing microbiome science through standardized fabricated ecosystems. *Nature methods*, 16(7), 567-571.